



DOI: [10.29026/oea.2025.240239](https://doi.org/10.29026/oea.2025.240239)

CSTR: [32247.14.oea.2025.240239](https://cstr.net.cn/32247.14.oea.2025.240239)

Phase reconstruction via metasurface-integrated quantum analog operation

Qiuying Li, Mingguang Liang, Shuoqing Liu, Jiawei Liu, Shizhen Chen, Shuangchun Wen and Hailu Luo*

Laboratory for Spin Photonics, School of Physics and Electronics, Hunan University, Changsha 410082, China.

*Correspondence: HL Luo, E-mail: hailuluo@hnu.edu.cn

This file includes:

[Section 1: Theoretical derivation of phase reconstruction](#)

[Section 2: Metasurface-based broadband differential operation](#)

[Section 3: Quality detection of polarization interferences](#)

[Section 4: Internal structure of beam splitter system](#)

[Section 5: Design and construction of metasurface](#)

[Section 6: Polarization conversion rates of metasurface](#)

[Section 7: Resolution analysis](#)

[Section 8: Sample preparation](#)

[Section 9: Error analysis](#)

Supplementary information for this paper is available at <https://doi.org/10.29026/oea.2025.240239>



Open Access This article is licensed under a Creative Commons Attribution 4.0 International License.

To view a copy of this license, visit <http://creativecommons.org/licenses/by/4.0/>.

© The Author(s) 2025. Published by Institute of Optics and Electronics, Chinese Academy of Sciences.

Section 1: Theoretical derivation of phase reconstruction

In our proposed metasurface-integrated quantum analog operation system, the metasurface and the polarization selection are the core of constructing differential operators. Firstly, the optical structure of the metasurface should be elucidated. As shown in Fig. 1(a) of the manuscript, there are four different working regions on the metasurface, and each region corresponds to a spatial differential operator. In each region, the optical axis distribution is anisotropic, and the local optical axis direction is $\eta(\mathbf{r}) = \pi|\mathbf{r}|/\Lambda$, where Λ is the grating period and the position vector $\mathbf{r} = \mathbf{x} + \mathbf{y}$. In the up region, the optical axis varies in the x -direction. While in the descending down region, the optical axis varied in the y -direction. The transmission matrix of any region can be expressed as

$$T = \begin{bmatrix} \cos\frac{v}{2} - i\sin\frac{v}{2}\cos 2\eta & -i\sin\frac{v}{2}\sin 2\eta \\ -i\sin\frac{v}{2}\sin 2\eta & \cos\frac{v}{2} + i\sin\frac{v}{2}\cos 2\eta \end{bmatrix}, \quad (S1)$$

where v is the uniform phase delay introduced by the metasurface. Supposing that the polarization wave function of the input photon is $|\Psi_{\text{pol}}\rangle_{\text{in}}$, owing to the spin basis $|+\rangle/|-\rangle$ forms an orthonormal complete system, in the spin basis, $|\Psi_{\text{pol}}\rangle_{\text{in}}$ can be expressed as

$$|\Psi_{\text{pol}}\rangle_{\text{in}} = A_+|+\rangle + A_-|-\rangle, \quad (S2)$$

where the expansion coefficient is $A_{\pm} = \langle \pm | \Psi_{\text{pol}} \rangle$. After passing the metasurface, the polarization wave function $|\Psi_{\text{pol}}\rangle_{\text{in}}$ will be converted to

$$|\Psi_{\text{pol}}\rangle_{\text{MS}} = T|\Psi_{\text{pol}}\rangle_{\text{in}} = B_+|+\rangle + B_-|-\rangle, \quad (S3)$$

where the expansion coefficient B_{\pm} can be calculated as

$$B_{\pm} = A_{\pm}\cos\frac{v}{2} - A_{\mp}i\sin\frac{v}{2}\exp(\mp i2\eta). \quad (S4)$$

For all photons to have a geometric phase attached by the spin-orbit interaction, the metasurface is designed with a half-wave phase delay, i.e., $v = \pi$, where the spins of all photons are reversed and can be expressed as

$$|\mp\rangle \rightarrow \exp(i\Phi_{\text{PB}})|\pm\rangle, \quad (S5)$$

here, $\Phi_{\text{PB}}(\mathbf{r}) = -\sigma_{\pm}2\eta(\mathbf{r})$ represents the geometric PB phase which is related to polarization. The geometric PB phase of different spatial components of photons indicate that the evolution process of polarization state is not uniform, which inevitably produces a geometric phase gradient and induces momentum shift ref.^{S1}

$$\Delta\mathbf{k} = \nabla\Phi_{\text{PB}} = -\sigma_{\pm}\frac{2\pi}{\Lambda}\mathbf{e}_r. \quad (S6)$$

Eventually, the momentum shift $\Delta\mathbf{k}$ causes the photon to produce a spin-dependent shift $\Delta\mathbf{r} = (\Delta\mathbf{k}/k_0)z = -\sigma_{\pm}(\lambda z/\Lambda)\mathbf{e}_r$ in real space that increases linearly with the transmission distance z , where $k_0 = 2\pi/\lambda$ represents the wave number and λ represents the central wavelength. By designing a sufficiently large grating period, the photons can generate a displacement in real space that is much smaller than the wave function width w , i.e. $|\Delta\mathbf{r}| \ll w$. Therefore, even though the photon with the polarizations $|+\rangle$ and $|-\rangle$ produce the shift in the opposite direction, the wave functions maintain a high overlap, so the interference effect in the overlapping region causes the photon to keep the original polarization state $|\Psi_{\text{pol}}\rangle_{\text{in}}$.

In our system, all photons are inputted to the metasurface and pre-selected to be H -polarized. In order to construct the spatial differential operator, it is also necessary to set the V -polarization selection at the back end of the metasurface. Here, in the spin basis, H - and V -polarization can be expressed as

$$|H\rangle = \frac{1}{\sqrt{2}}(|+\rangle + |-\rangle), \quad |V\rangle = \frac{-i}{\sqrt{2}}(|+\rangle - |-\rangle). \quad (S7)$$

The total wave function of photons can be expressed as the product of space and polarization wave function

$$|\Psi_{\text{tot}}\rangle_{\text{in}} = |\Psi_{\text{sp}}(\mathbf{r})\rangle \otimes |\Psi_{\text{pol}}\rangle_{\text{in}}. \quad (S8)$$

After passing through the metasurface, the wave function of the H -polarized image photon can be written as

$$|\Psi_{\text{tot}}\rangle_{\text{MS}} = \frac{1}{2} \exp(-i2\eta) |\Psi_{\text{sp}}(\mathbf{r} - \Delta\mathbf{r})\rangle |+\rangle + \frac{1}{2} \exp(i2\eta) |\Psi_{\text{sp}}(\mathbf{r} + \Delta\mathbf{r})\rangle |-\rangle. \quad (\text{S9})$$

After V -polarization selection, the final output wave function can be expressed as

$$|\Psi_{\text{tot}}\rangle_{\text{out}} = \frac{i}{2} [\exp(-i2\eta) |\Psi_{\text{sp}}(\mathbf{r} - \Delta\mathbf{r})\rangle - \exp(i2\eta) |\Psi_{\text{sp}}(\mathbf{r} + \Delta\mathbf{r})\rangle] |V\rangle. \quad (\text{S10})$$

Specially, in the spatial differentiation, we are only concerned with the spatial part of the output wave function

$$|\Psi_{\text{sp}}\rangle_{\text{out}} = \frac{i}{2} [\exp(-i2\eta) |\Psi_{\text{sp}}(\mathbf{r} - \Delta\mathbf{r})\rangle - \exp(i2\eta) |\Psi_{\text{sp}}(\mathbf{r} + \Delta\mathbf{r})\rangle]. \quad (\text{S11})$$

In each working region, the direction of the optical axis through which the image photon passes are different. In the four regions, the angles between the optical axis and the horizontal direction are $\eta_1 = \alpha$, $\eta_2 = -\alpha$, $\eta_3 = \pi/2 - \beta$, $\eta_4 = \pi/2 + \beta$, respectively, where $\alpha, \beta \rightarrow 0$. Thus, the four geometric phase terms can be represented as

$$\begin{cases} \exp(\pm i2\eta_1) = \cos\eta_1 \pm i\sin\eta_1 \approx 1 \pm i\eta_1 = 1 \pm i\alpha \\ \exp(\pm i2\eta_2) = \cos\eta_2 \pm i\sin\eta_2 \approx 1 \pm i\eta_2 = 1 \mp i\alpha \\ \exp(\pm i2\eta_3) = \cos\eta_3 \pm i\sin\eta_3 \approx \left(\frac{\pi}{2} - \eta_3\right) \pm i = \beta \pm i \\ \exp(\pm i2\eta_4) = \cos\eta_4 \pm i\sin\eta_4 \approx \left(\frac{\pi}{2} - \eta_4\right) \pm i = -\beta \pm i \end{cases}. \quad (\text{S12})$$

If the imaging photon passes through region 1, $|\Psi_{\text{sp}}\rangle_{\text{out}}$ can be approximated to

$$\begin{aligned} |\Psi_{\text{sp}}\rangle_{\text{out}}^{(1)} &\approx \frac{i}{2} [(1 - i\alpha) |\Psi_{\text{sp}}(x - \delta, y)\rangle - (1 + i\alpha) |\Psi_{\text{sp}}(x + \delta, y)\rangle] \\ &= \frac{i}{2} \{ [|\Psi_{\text{sp}}(x - \delta, y)\rangle - |\Psi_{\text{sp}}(x + \delta, y)\rangle] - i\alpha [|\Psi_{\text{sp}}(x - \delta, y)\rangle + |\Psi_{\text{sp}}(x + \delta, y)\rangle] \}, \end{aligned} \quad (\text{S13})$$

In the case of $\delta \rightarrow 0$, the following approximation exists in the linear combination of functions:

$$\begin{cases} \lim_{\delta \rightarrow 0} [|\Psi_{\text{sp}}^e(x + \delta, y)\rangle_{\text{in}} + |\Psi_{\text{sp}}^e(x - \delta, y)\rangle_{\text{in}}] = 2|\Psi_{\text{sp}}^e(x, y)\rangle_{\text{in}} \\ \lim_{\delta \rightarrow 0} [|\Psi_{\text{sp}}^e(x + \delta, y)\rangle_{\text{in}} - |\Psi_{\text{sp}}^e(x - \delta, y)\rangle_{\text{in}}] = 2\delta \frac{\partial |\Psi_{\text{sp}}^e(x, y)\rangle_{\text{in}}}{\partial x} \end{cases}. \quad (\text{S14})$$

Consequently, Eq. (S13) can be rewritten as

$$|\Psi_{\text{sp}}\rangle_{\text{out}}^{(1)} \approx -i\delta \frac{\partial |\Psi_{\text{sp}}(x, y)\rangle}{\partial x} - \alpha |\Psi_{\text{sp}}(x, y)\rangle \propto \left[\alpha + i\delta \frac{\partial}{\partial x} \right] |\Psi_{\text{sp}}(x, y)\rangle. \quad (\text{S15})$$

The same is true for the other three regions. The whole process can be expressed as the differential operator \hat{F}_i constructed by the hypersurface and the polarization analyzer before and after it applies to the input spatial wave function $|\Psi_{\text{sp}}(x, y)\rangle$, that is

$$\begin{cases} |\Psi_{\text{sp}}\rangle_{\text{out}}^{(1)} = \hat{F}_1 |\Psi_{\text{sp}}(x, y)\rangle \propto \left[\alpha + i\delta \frac{\partial}{\partial x} \right] |\Psi_{\text{sp}}(x, y)\rangle \\ |\Psi_{\text{sp}}\rangle_{\text{out}}^{(2)} = \hat{F}_2 |\Psi_{\text{sp}}(x, y)\rangle \propto \left[\alpha - i\delta \frac{\partial}{\partial x} \right] |\Psi_{\text{sp}}(x, y)\rangle \\ |\Psi_{\text{sp}}\rangle_{\text{out}}^{(3)} = \hat{F}_3 |\Psi_{\text{sp}}(x, y)\rangle \propto \left[\beta + i\delta \frac{\partial}{\partial y} \right] |\Psi_{\text{sp}}(x, y)\rangle \\ |\Psi_{\text{sp}}\rangle_{\text{out}}^{(4)} = \hat{F}_4 |\Psi_{\text{sp}}(x, y)\rangle \propto \left[\beta - i\delta \frac{\partial}{\partial y} \right] |\Psi_{\text{sp}}(x, y)\rangle \end{cases} \quad (\text{S16})$$

After the action of four differential operators, the probability density of the output wave function is displayed on the imaging plane:

$$\left\{ \begin{array}{l} P_{\text{out}}^{(1)}(x, y) = \langle \Psi_{\text{sp}} | \Psi_{\text{sp}} \rangle_{\text{out}}^{(1)} \approx \cos^2 \gamma P_{\text{in}}(x, y) \left\{ \alpha^2 + \left[\delta \frac{\partial \varphi(x, y)}{\partial x} \right]^2 - 2\alpha \delta \frac{\partial \varphi(x, y)}{\partial x} \right\} \\ P_{\text{out}}^{(2)}(x, y) = \langle \Psi_{\text{sp}} | \Psi_{\text{sp}} \rangle_{\text{out}}^{(2)} \approx \cos^2 \gamma P_{\text{in}}(x, y) \left\{ \alpha^2 + \left[\delta \frac{\partial \varphi(x, y)}{\partial x} \right]^2 + 2\alpha \delta \frac{\partial \varphi(x, y)}{\partial x} \right\} \\ P_{\text{out}}^{(3)}(x, y) = \langle \Psi_{\text{sp}} | \Psi_{\text{sp}} \rangle_{\text{out}}^{(3)} \approx \sin^2 \gamma P_{\text{in}}(x, y) \left\{ \beta^2 + \left[\delta \frac{\partial \varphi(x, y)}{\partial x} \right]^2 - 2\beta \delta \frac{\partial \varphi(x, y)}{\partial x} \right\} \\ P_{\text{out}}^{(4)}(x, y) = \langle \Psi_{\text{sp}} | \Psi_{\text{sp}} \rangle_{\text{out}}^{(4)} \approx \sin^2 \gamma P_{\text{in}}(x, y) \left\{ \beta^2 + \left[\delta \frac{\partial \varphi(x, y)}{\partial x} \right]^2 + 2\beta \delta \frac{\partial \varphi(x, y)}{\partial x} \right\} \end{array} \right. , \quad (\text{S17})$$

where $P_{\text{in}}(x, y) = \langle \Psi_{\text{sp}} | \Psi_{\text{sp}} \rangle$ represents the initial probability density of the imaging photon, γ represents the initial polarization angle of the imaging photon. Subtracting $P_{\text{out}}^{(1)}(x, y)$ and $P_{\text{out}}^{(2)}(x, y)$ to get

$$\Delta P_{\text{out}}^x(x, y) \approx 2\alpha \delta \cos^2 \gamma P_{\text{in}}(x, y) \frac{\partial \varphi(x, y)}{\partial x} . \quad (\text{S18})$$

Subsequently, Subtracting the equations $P_{\text{out}}^{(3)}(x, y)$ and $P_{\text{out}}^{(4)}(x, y)$ to get

$$\Delta P_{\text{out}}^y(x, y) \approx 2\beta \delta \sin^2 \gamma P_{\text{in}}(x, y) \frac{\partial \varphi(x, y)}{\partial y} . \quad (\text{S19})$$

Eventually, the quantitative phase gradient can be expressed as

$$\nabla \varphi(x, y) = \frac{\partial \varphi(x, y)}{\partial x} \mathbf{e}_x + \frac{\partial \varphi(x, y)}{\partial y} \mathbf{e}_y = \frac{\Delta P_{\text{out}}^x(x, y)}{2\alpha \delta \cos^2 \gamma P_{\text{in}}(x, y)} \mathbf{e}_x + \frac{\Delta P_{\text{out}}^y(x, y)}{2\beta \delta \sin^2 \gamma P_{\text{in}}(x, y)} \mathbf{e}_y . \quad (\text{S20})$$

Section 2: Metasurface-based broadband differential operation

In the proposed system, the metasurface used for optical differentiation is broadband, and the imaging results are almost not limited by the working wavelength. According to Eq. (S4), the effect of a metasurface on the polarization states of left- (LCP) and right-handed circularly polarized (RCP) photons with arbitrary wavelength can be expressed as

$$\begin{pmatrix} 1 \\ \sigma_{\pm} \mathbf{i} \end{pmatrix} \rightarrow \cos \frac{v}{2} \begin{pmatrix} 1 \\ \sigma_{\pm} \mathbf{i} \end{pmatrix} + i \sin \frac{v}{2} \begin{pmatrix} 1 \\ \sigma_{\mp} \mathbf{i} \end{pmatrix} e^{i2\sigma_{\pm} \alpha(x, y)} , \quad (\text{S21})$$

here, $\sigma = \pm 1$ represents LCP and RCP states, v represents the birefringent phase delay of the metasurface, and $\alpha(x, y)$ is the direction of optical axes on the metasurface. When the input photon is at the working wavelength ($\lambda = 810$ nm), the polarization states of the LCP and RCP photons are completely reversed and a tiny opposite shift can also be generated in real space. In the case of photons passing through the 0° local optical axis of the metasurface, the overlap of the LCP and RCP components maintains the original linear polarization state. In our optical differential operation system, there is a linear polarizer after the metasurface orthogonal to the input polarization state to eliminate the spatial overlap of the LCP and RCP components and perform differential operations [Fig. S1]. However, if the input photon is not at the correct working wavelength ($v \neq \pi$), such as 633 nm, the differential operation can still be performed normally^{S2}. In this case, the photon output from the metasurface has a certain probability of maintaining the original polarization state and propagation direction. Subsequently, this part of the photon will be eliminated by the linear polarizer at the back end of the metasurface, the result of the differential operation is not affected except for the attenuation of the light intensity.

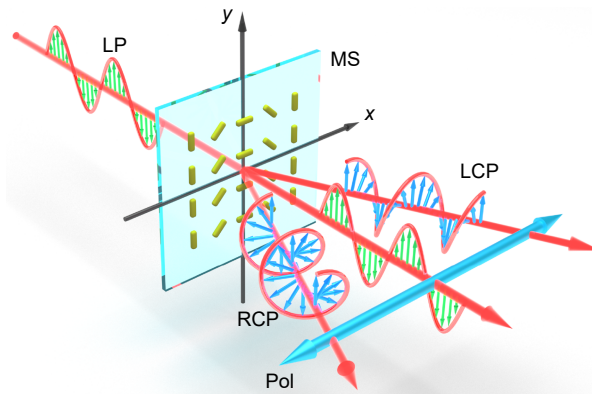


Fig. S1 | Schematic diagram of the implementation of differential operations on a metasurface. LP, linear polarization; MS, metasurface; LCP, left-handed circularly polarized; RCP, right-handed circularly polarized; Pol, linear polarizer.

Section 3: Quality detection of polarization interferences

A 405 nm wavelength laser is pumped into the BBO crystal, and the type-I spontaneous parametric down conversion (SPDC) results in the generation of a pair of photons, which are a signal photon and an idler photon. The experimental setup is shown in Fig. S1, the input two-photon polarization entanglement generated by BBOs can be expressed as $|\phi^+\rangle = (1/\sqrt{2})(|H_i\rangle|H_t\rangle + |V_i\rangle|V_t\rangle)$ ^{S3,S4}. Counting the two-photon coincidence under the polarization interference can perform the quality of the entangled source. Specifically, one polarizer is fixed as 0° or 45° , the other polarizer is rotated from 0° to 180° in the step of 10° , the two-photon coincidence counts are recorded under per rotation of the polarizer. Finally, the two sinusoidal curves, which representing the relationship between rotation angles and coincidence counts, are fitted as shown the inset in Fig. S2. Besides, the equation about interference visibility can be expressed as

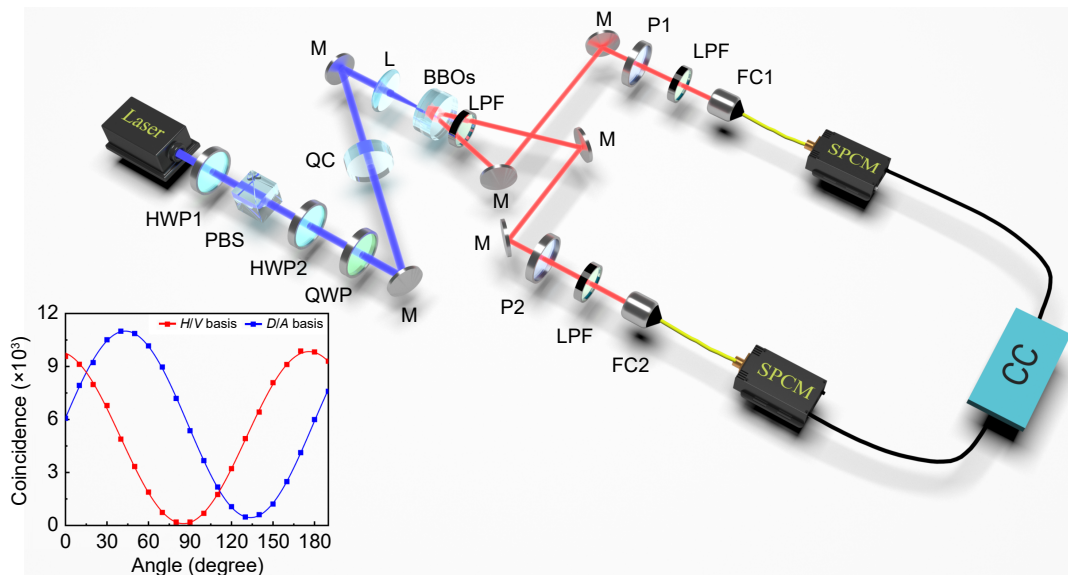


Fig. S2 | Experimental setup of the quality detection of polarization interferences. Setup schematic: HWP, half-wave plate; QWP, quarter-wave plate; PBS, polarizing beam splitter; M, mirror; QC, quartz crystal; L, Lens; BBOs, β -BaB₂O₄ crystals; LPF, long-pass filter; FC, fiber coupler; SPCM, single photon counting module; CC, coincidence counts device. Inset, the experimental results of polarization interferences.

$$\mathcal{V} = \frac{C_{\max} - C_{\min}}{C_{\max} + C_{\min}}, \quad (\text{S22})$$

where C_{\min} and C_{\max} indicate the minimum and maximum coincidence counts, respectively. In the H/V and D/A bases, the interference visibility can be calculated as $(97.90 \pm 0.04)\%$ and $(92.23 \pm 0.30)\%$, respectively, which are outper-

form the visibility limit needed to violate the Bell's inequality of 71%^{S5,S6}. Here, $|D\rangle = (1/\sqrt{2})(|H\rangle + |V\rangle)$ and $|A\rangle = (1/\sqrt{2})(|H\rangle - |V\rangle)$ denote the linearly polarized states with polarization angles of 45° and -45° , respectively. Therefore, the two-photon entanglement source generated by type-I SPDC in our experiment meets the requirement of quantum imaging.

Section 4: Internal structure of beam splitter system

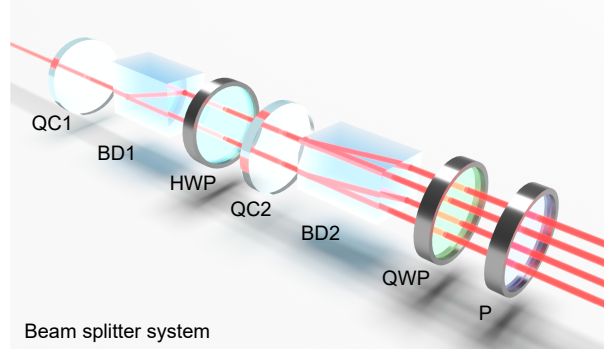


Fig. S3 | Internal structure of beam splitter. The experimental setup of beam splitter system. QC, quartz crystal; BD, beam displacers; HWP, half-wave plate; QWP, quarter-wave plate; P, polarizer.

As shown in Fig. S2, the 2×2 beam splitter system is consisted of two beam displacers (BD), a half-wave plate (HWP), a quarter-wave plate (QWP), and a polarizer (P), which can evenly divide a 45° linearly polarized light into four horizontally polarized light beams. Since the propagation phase is dependent on the optical path, the four channels should share the same optical path for the incident waves. To ensure such condition in the experiment, two quartz crystals (QC) are inserted into the beam splitter system.

Firstly, the function of the QC is explained, which is to compensate the optical path difference between the H and V components of the beam caused by BD. Here, the BD is a uniaxial birefringent negative crystal with different principal refractive indices for ordinary ray (o-ray) and extraordinary ray (e-ray). In particular, for the o- and e-ray with a wavelength of 810 nm, the main refractive indices are n_{co} and n_{ce} , respectively. When a calcite crystal is used to manufacture BD, the angle between the optical axis and the normal of the light surface is designed to be θ , which allows the e-ray to produce a discrete angle α relative to the o-ray. According to the theory of crystal optics, α can be calculated by the Eq. (S23)^{S7}

$$\tan\alpha = \left(1 - \frac{n_{co}^2}{n_{ce}^2}\right) \frac{n_{ce}^2 \tan\theta}{n_{ce}^2 + n_{co}^2 \tan^2\theta}. \quad (\text{S23})$$

Due to birefringence effect, o-ray and e-ray produce optical a path difference ΔL inside BD, which can be calculated as:

$$\Delta L = \frac{n_2 L}{\cos\alpha} - n_1 L. \quad (\text{S24})$$

here, L is the radial length of BD, n_1 and n_2 are the refractive indices of o- and e-ray in BD, respectively, which can be expressed as^{S7}

$$n_1 = n_{co}, \quad n_2 = \frac{n_{co}^2 n_{ce}^2}{n_{co}^2 \sin^2\theta + n_{ce}^2 \cos^2\theta}. \quad (\text{S25})$$

To compensate for the optical path difference caused by BD, a QC with an optical axis perpendicular to the surface is used with two principal refractive indices n_{qo} and n_{qe} . Since the QC is also a uniaxial birefringent negative crystal, its main section needs to be orthogonal to the main section of BD when compensating for the optical path difference. In this basis, the desired thickness of QC is calculated to be $D = \Delta L / (n_{qe} - n_{qo})$.

Secondly, the working principle of the beam splitter system is explained. The optical axis of BD1 is in the vertical

plane, so H - and V -polarized light are o- and e-ray in BD1, respectively. At the output end of BD1, the V -polarized light generates a lateral displacement $d = L\cos\alpha$, which realizes the two-beam splitting of the incident light. Subsequently, a HWP converts H - and V -polarized light to 45° and -45° polarized light, respectively. Different from BD1, the optical axis of BD2 is in the horizontal plane, and eventually the 2 beams will further be split into 4 beams and be arranged 2×2 . In order to convert all output light to horizontal polarization, a 45° QWP and horizontal polarizer are used at the back end of the BD2.

Section 5: Design and construction of metasurface

As shown in Fig. S4(a), the metasurface is made of fused quartz glass (SiO_2) and has a one-inch light-through aperture, where the orange box indicates the working area. As shown in Fig. S4(b–d), the working area of the metasurface is divided into four parts. In order to realize the spatial differential operation, some nanogrooves with periodic spatial changes are carved on the surface of each working area by femtosecond laser as optical axes. Under intense laser irradiation, the uniform quartz glass breaks down into porous glass ($\text{SiO}_{2(1-x)} + \text{O}_2$), and the refractive index depends on the laser intensity. Therefore, the raster-like nanostructures can be generated to create birefringent effects in isotropic glass samples. The directions of local optical axis (fast and slow) are perpendicular and parallel to the grooves respectively. Since the characteristic size of the structure is much smaller than the operating wavelength, the fabricated metamaterial can be viewed as a birefringent wave plate with uniform phase delay and anisotropy in the direction of the optical axis.

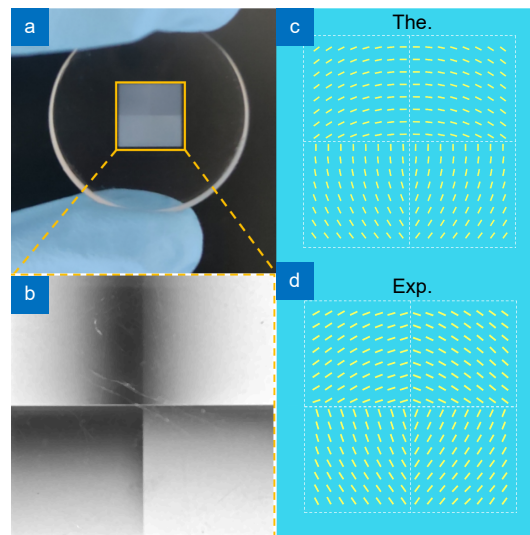


Fig. S4 | Design and construction of metasurface. (a) Image of the metasurface. (b) Metasurface morphology under orthogonal polarizer. (c) Theoretical design image of optical axes. (d) Experimentally measured distribution of optical axes.

Section 6: Polarization conversion rates of metasurface

The metasurface can be fabricated by femtosecond laser-writing spatially varying nanogrooves in fused silica samples. The laser beam is focused 200 μm below the surface of the glass sample. Under intense laser irradiation, the homogeneous glass (SiO_2) decomposes into porous glass ($\text{SiO}_{2(1-x)} + \text{O}_2$), whose refractive index depends on the laser intensity. Therefore, periodic variations of the intensity enable modulation of the refractive index; i.e., grating-like nanostructures can be produced, creating a birefringent effect in isotropic glass samples. By designing a local optical axis that varies periodically in one dimension and a uniform half-wave birefringent phase delay, the metasurface enables the exchange of polarization states between left- and right-handed circularly polarized light. To measure the polarization conversion ratio (PCR) in this process, we performed the experiment shown in Fig. S5(a). In the experiment, P1 was fixed at 0° , both QWPs were set to 45° , and P2 was switched between 0° and 90° to detect converted and unconverted light. Consequently, the PCR can be calculated according to Eq. (S26)

$$\text{PCR} = \left(1 - \frac{I_{\text{unconverted}}}{I_{\text{converted}}}\right) \times 100\%, \quad (\text{S26})$$

As a result, the four channels of the metasurface were shown to have high PCRs ranging from 96% to 97% [Fig. S5(b–e)].

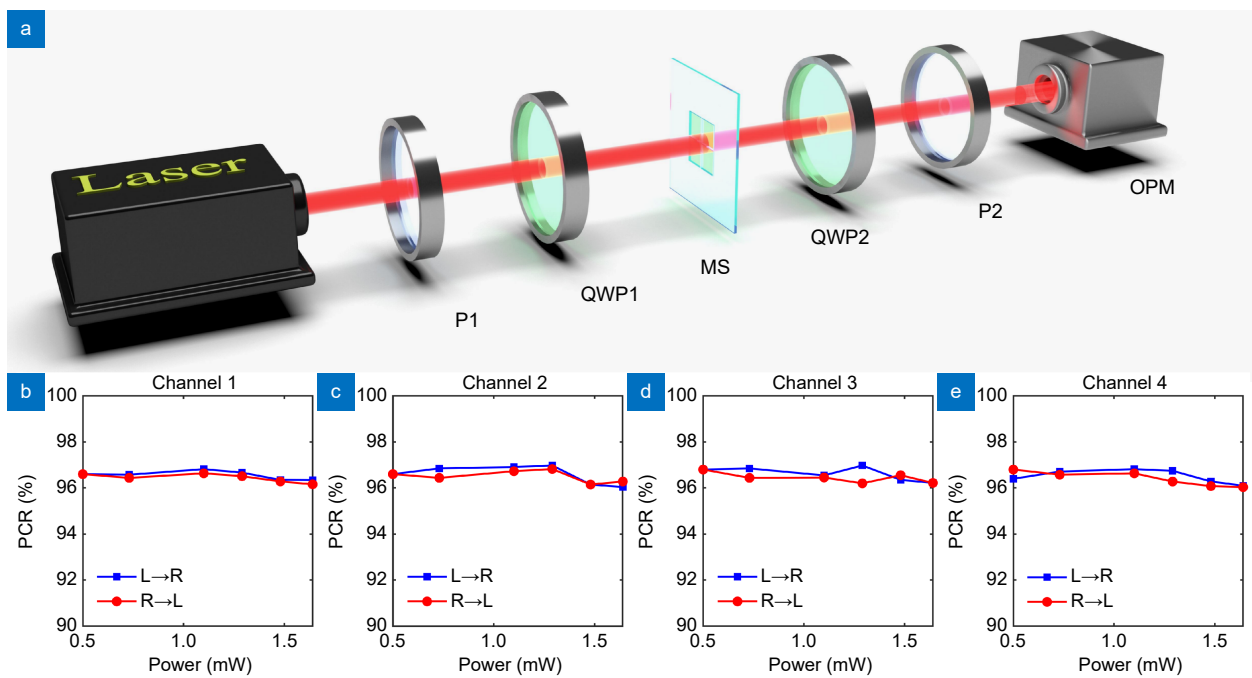


Fig. S5 | Experimental measurements of PCR. (a) Experimental setup. Laser, 810 nm continuous laser; P, linear polarizer; QWP, quarter-wave plate; MS, metasurface; OPM, optical power meters. (b–e) Measurements of the polarization transition rate for the four channels of the metasurface.

Section 7: Resolution analysis

In order to evaluate the resolution of our imaging system, data analyses were performed on the differential edge results [Fig. S6(a) and S6(b)], where the polarization selectors before and after the metasurface are set to be orthogonal. As shown in Fig. S6(c) and S6(d), normalized intensity distributions are obtained by taking cross sections along an arbitrary white dashed line in Fig. S6(a) and S6(b), respectively. To calculate the resolution, Gaussian line spread function (LSF) is chosen to fit the data, which can be expressed as ref.^{S8}:

$$\text{LSF}(r) = \frac{2a}{\sqrt{\pi w^2}} \exp \left[-\frac{(r - r_0)^2}{w^2} \right], \quad r = x, y, \quad (\text{S27})$$

where a , r_0 and w are fit parameters. Consequently, the resolution of the imaging system can be calculated as the full width at half maximum (FWHM) of the LSF, i.e., $\mathcal{R} = 2\sqrt{\ln 2}w$. Ultimately, the resolution of our imaging system was calculated as the average of the FWHM of the four characteristic peaks of 52.99 μm .

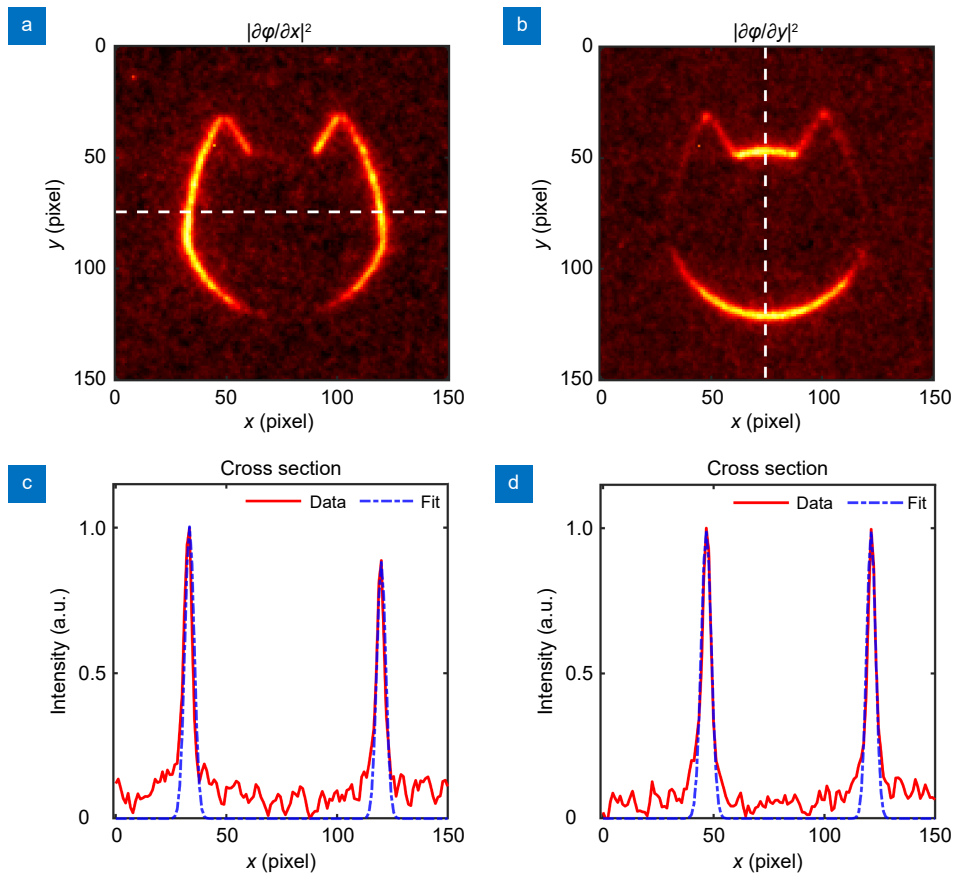


Fig. S6 | Resolution analysis. (a, b) Results of differential operations in the x and y directions for the shape “cat”. (c, d) are the normalized intensity distributions along the white dashed cross section and the fit to the Gaussian line spread function in (a) and (b), respectively.

Section 8: Sample preparation

To verify the feasibility of metasurface-integrated quantum analog operation system in quantitative phase reconstruction, the JGS2 quartz glass was used as the sample substrate, and different patterns were etched on the substrate by chemical method [Fig. S7(a)]. In the red dashed box in Fig. S7(a), the etching depths of "Cat" is only designed to be 400 nm, "01" has two depth distributions of 200 nm and 400 nm, and "Tai Chi" has three depth distributions of 200 nm, 400 nm, and 600 nm, respectively [Fig. S7(b)]. Ultimately, a probe scan is performed along the blue dashed line shown in Fig. S7(b) to examine the accuracy of the etch depth [Fig. S7(c)].

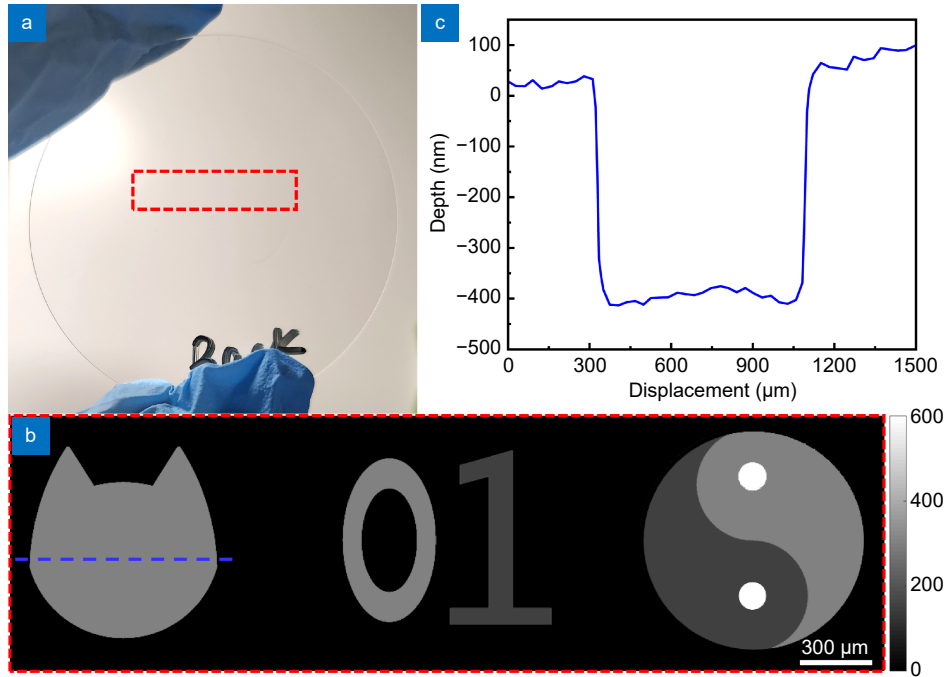


Fig. S7 | Information for the phase object samples. (a) Physical drawings. (b) Design drawings. (c) Probe scanning results along the blue dashed line in (b).

Section 9: Error analysis

In the quantitative phase reconstruction scheme, the target object has etching depths of 200, 400 and 600 nm. The accuracy of quantitative phase reconstruction can be described.

$$\vartheta = \sum_{i=1}^N \frac{|\varphi_i^R - \varphi_i^M|}{N\varphi_i^R} \times 100\%, \quad (\text{S28})$$

here, φ_i^R and φ_i^M represent the true value and the measured value of the phase respectively, and N is the number of data points.

In our quantitative phase reconstruction scheme, the differential operations are needed to perform. The following approximations are used in the construction of differential operators

$$\begin{aligned} \frac{\partial \varphi(x, y)}{\partial x} &\approx \frac{\varphi(x + \delta, y) - \varphi(x - \delta, y)}{2\delta}, \\ \frac{\partial \varphi(x, y)}{\partial y} &\approx \frac{\varphi(x, y + \delta) - \varphi(x, y - \delta)}{2\delta}, \end{aligned} \quad (\text{S29})$$

where δ represents the spin dependent displacement of the photon. It can be seen that the smaller the δ , the closer the measured phase gradient is to the true value. Meanwhile, the resolution of ICCD also has some influence on the above approximation.

Subsequently, the measured value $\nabla \varphi(x, y)$ is related to the polarization angle of the image photon, the local optical

axis direction of the metasurface, and the initial probability distribution. The polarization angle of the imaging photon is non-locally controlled by the trigger photon, in this process, if the quality of the entanglement source is not superior, the imaging photon may not be induced to the desired state by the trigger photon. In addition, the local optical axes direction of the metasurface is affected by the alignment of the optical path, so the alignment of the optical path is also an influencing factor on the accuracy. In order to obtain the initial probability distribution, the polarization selection at the back end of the metasurface needs to be rotated by 90° , which may cause some optical path deflection and may also affect the accuracy of quantitative phase reconstruction. Finally, the normalized phase distribution is calculated by Fourier transform. Then the normalized coefficient is obtained by solving the optimization problem, and the quantitative phase reconstruction can be further obtained. The above algorithm includes Fourier transform and optimization problem, and the optimization of the algorithm is helpful to improve the accuracy of quantitative reconstruction.

References

- S1. Ling XH, Zhou XX, Yi XN et al. Giant photonic spin hall effect in momentum space in a structured metamaterial with spatially varying birefringence. *Light Sci Appl* 4, e290 (2015).
- S2. Zhou JX, Qian HL, Zhao JX et al. Two-dimensional optical spatial differentiation and high-contrast imaging. *Natl Sci Rev* 8, nwa176 (2021).
- S3. Kwiat PG, Waks E, White AG et al. Ultrabright source of polarization-entangled photons. *Phys Rev A* 60, R773–R776 (1999).
- S4. Kong LJ, Sun YF, Zhang FR et al. High-dimensional entanglement-enabled holography. *Phys Rev Lett* 130, 053602 (2023).
- S5. Clauser JF, Shimony A. Bell's theorem. Experimental tests and implications. *Rep Prog Phys* 41, 1881–1927 (1978).
- S6. Horodecki R, Horodecki P, Horodecki M et al. Quantum entanglement. *Rev Mod Phys* 81, 865 (2009).
- S7. Hecht E. *Optics, Global Edition* 5th ed (Pearson Higher Education, London, 2016).
- S8. He Z, Zhang YD, Tong X et al. Quantum microscopy of cells at the Heisenberg limit. *Nat Commun* 14, 2441 (2023).